

# Experimental realization of the devil's vortex Fresnel lens with a programmable spatial light modulator

Mark Mitry,<sup>1</sup> Danielle C. Doughty,<sup>1</sup> Jan L. Chaloupka,<sup>2</sup> and Matthew E. Anderson<sup>1,\*</sup>

<sup>1</sup>Department of Physics, San Diego State University, San Diego, California 92182, USA

<sup>2</sup>Department of Physics, University of Northern Colorado, Greeley, Colorado 80639, USA

\*Corresponding author: matt@sciences.sdsu.edu

Received 23 February 2012; revised 19 April 2012; accepted 19 April 2012;  
posted 19 April 2012 (Doc. ID 163561); published 14 June 2012

We present a unique method for experimentally generating multiple vortices by way of a devil's vortex lens combined with a Fresnel lens using a spatial light modulator. These lenses have the multifocal properties of fractal zone plates combined with the orbital angular momentum of a spiral phase plate and can be tailored to fit within a small space on an optical bench. Results are presented alongside numerical simulations, demonstrating the robust nature of both the experimental method and the predictive power of the Huygens–Fresnel wavelet theory. © 2012 Optical Society of America

OCIS codes: 050.4865, 050.1950.

## 1. Introduction

Optical vortices describe points of singularity in the electromagnetic field where the intensity vanishes. These arise from the destructive interference of electric fields that have phases that ramp from zero to an integer multiple of  $2\pi$  in the immediate vicinity of the singularity. Such singularities in the electromagnetic field were discussed as far back as 1931 [1]. The topic gained new momentum, however, with the seminal paper on dislocations in wave trains by Nye and Berry [2] and the demonstration that optical vortex beams of light actually carry orbital angular momentum [3]. With the introduction of the computer-generated spiral phase plate [4] and its dynamic and programmable counterpart, the liquid crystal spatial light modulator [5], optical vortices have garnered even more attention. Demonstrations have included the ability to trap and rotate particles [6], create micromechanical pumps [7], store quantum information [8], enhance microscopy [9] and

scanning techniques [10], and much more (see, for instance, [11]).

The production of multiple vortices occupying different axial regions simultaneously is of interest to both the trapping and imaging community. One such approach to producing multiple focal spots is with the use of a fractal zone plate [12,13], and multiple vortices may be realized through a spiral fractal zone plate [14]. These demonstrated zone plates were binary, however, which severely limits their diffraction efficiency. It is possible to overcome this hindrance by the use of a blazed fractal zone plate, the so-called devil's lens [15,16]. These phase plates make use of the fractal Cantor set, also known as the devil's staircase [17,18], in which the radial phase distribution exhibits a ramped stair-step pattern. With the further incorporation of a spiral phase plate, it was proposed that the devil's vortex lens (DVL) [19] would be able to generate multiple axial vortices simultaneously.

We present the experimental realization of the DVL via a programmable spatial light modulator. It is observed that multiple vortices are indeed generated, and the resulting axial and transverse

beam distributions are carefully measured and compared to numerical predictions, exhibiting excellent agreement.

## 2. DVL Theory

A devil's lens is based on the one-dimensional Cantor function, which is a particular case of a devil's staircase. Its domain is  $[0, 1]$  and is formed by the removed segments of the ternary Cantor set, which is conceptually made by taking a line segment and removing the middle third repeatedly for all remaining segments. The Cantor function is defined as

$$F_s(x) = \begin{cases} \frac{l}{2^s}, & \text{if } p_{s,l} \leq x \leq q_{s,l} \\ \frac{1}{2^s} \frac{x - q_{s,l}}{p_{s,l+1} - q_{s,l}} + \frac{l}{2^s}, & \text{if } q_{s,l} \leq x \leq p_{s,l+1} \end{cases}, \quad (1)$$

where  $s$  is the function order and  $l$  indicates the number of horizontal sections the function has and takes on the integer values from 0 to  $2^s - 1$  [19]. The values of  $q$  and  $p$  are the start and end points for each segment of the Cantor set, as described in [18]. For example,  $q_{s,l}$  and  $p_{s,l}$  for the first three values of  $s$  are given in Table (1). From each horizontal segment, the function  $F_s$  increases linearly from  $q_{s,l}$  to  $p_{s,l+1}$ . The graph of  $F_3(x)$  in Fig. 1(a), shows the function has seven horizontal sections, which means  $l = 0, \dots, 7$ .

In terms of the Cantor function  $F_s$ , the devil's lens (DL) function is defined as

$$Q_s(\zeta) = \exp[-i2^{s+1}\pi F_s(\zeta)], \quad \zeta = (r/a)^2, \quad (2)$$

where  $\zeta$  is the normalized quadratic radial coordinate and  $a$  is the lens radius. Similar to  $F_s$  in Fig. 1(a), the phase of  $Q_s(\zeta)$  will increase linearly from 0 to  $2\pi$  but will have jump discontinuities at every  $q_{s,l}$  where the phase is locked at 0 for the horizontal segments, except for the first point  $q_{s,0}$ . If a DL is plotted as a function of the normal radial coordinate  $r$ , the phase will instead increase quadratically from 0 to  $2\pi$  and the transition points will shift from  $(q \ \& \ p)$  to  $(\sqrt{q} \ \& \ \sqrt{p})$ . This quadratic phase variation can be seen in the plot of  $Q_3(r/a)$  in Fig. 1(b). As you can see, the outer concentric rings are more narrow than the inner ones.

A DVL is made by combining a spiral phase plate and a devil's lens. A DVL is the product of two functions, one being the radially dependent function  $Q_s(\zeta)$  and the other being an azimuthally dependent vortex function. The DVL function is defined as

$$\begin{aligned} \Phi_{s,m}(\zeta, \theta) &= \overbrace{Q_s(\zeta)}^{\text{radial}} \times \overbrace{V_m(\theta)}^{\text{azimuthal}}, \\ \Phi_{s,m}(\zeta, \theta) &= \exp[-i2^{s+1}\pi F_s(\zeta)] \exp[im\theta], \end{aligned} \quad (3)$$

where  $m$  is the topological vortex charge and  $\theta$  is the azimuthal angle. The vortex function adds an azimuthal phase variation that increases linearly from 0 to  $2\pi$  as  $\theta$  increases. Fig. 1(c) shows the phase variation of a DVL where  $s = 3$  and  $m = 1$ . The diffraction pattern from a DL ( $m = 0$ ) illuminated with monochromatic plane waves is a series of foci, with a major focus located at [19],

$$f_s = a^2 / 2l3^s. \quad (4)$$

For  $m \neq 0$ , each focus becomes doughnut shaped and the size of the hole increases as  $m$  increases. As  $s$  increases, the number of subsidiary foci increases. From Eq. (4), the main focal length becomes shorter as  $s$  increases. For a wavelength of 800 nm and a lens radius of 1 cm, the lengths of  $f_s$  for  $s = 1 \rightarrow 4$  are

$$\begin{aligned} f_1 &= 20.77 \text{ m}, & f_2 &= 6.92 \text{ m}, \\ f_3 &= 2.31 \text{ m}, & f_4 &= 0.77 \text{ m}. \end{aligned}$$

For a lab with limited space, these distances are unfeasible. One solution would be to use  $s$  values of 4 or greater, but this introduces another problem due to the limited resolution of our spatial light modulator (SLM). The SLM used is a  $768 \times 768$  pixel array with a pixel size of approximately  $26 \mu\text{m} \times 26 \mu\text{m}$ . Because the radial phase transition regions become more narrow as  $s$  increases, there is an upper limit to the order we can properly encode onto our LCD. By setting the minimum transition width to be twice our pixel size, the highest  $s$  value we can encode is  $s = 4$ . Therefore, in order to observe the diffraction patterns for  $s = 1 \rightarrow 4$  over a manageable distance, we incorporated a converging Fresnel lens into our DVL.

In the same way we incorporated a spiral phase function to a devil's lens, the same is done with a Fresnel lens. We use a converging Fresnel lens that is defined as

$$L_{f_0}(\zeta) = \exp[-i\pi\zeta a^2 / \lambda f_0], \quad (5)$$

where  $f_0$  is the focal length and  $\lambda$  is the incident wavelength. By combining  $L_{f_0}$  with our DVL in Eq. (3), our devil's vortex Fresnel lens (DVFL) becomes

$$\begin{aligned} \Omega_{s,m,f_0}(\zeta, \theta) &= Q_s(\zeta) \times V_m(\theta) \times L_{f_0}(\zeta), \\ \Omega_{s,m,f_0}(\zeta, \theta) &= \exp[-i2^{s+1}\pi F_s(\zeta)] \exp[im\theta] \\ &\quad \times \exp[-i\pi\zeta a^2 / \lambda f_0]. \end{aligned} \quad (6)$$

In Fig. 2, the phase plots of a DL, a spiral phase plate, and a Fresnel lens are summed together to form a

Table 1. Values of  $q_{s,l}$  and  $p_{s,l+1}$  for  $s=0, 1, 2$

$s = 0$	$q_{0,0}, p_{0,1}$	0, 1
$s = 1$	$q_{1,0}, p_{1,1}, q_{1,1}, p_{1,2}$	0, 1/3, 2/3, 1
$s = 2$	$q_{2,0}, p_{2,1}, q_{2,1}, p_{2,2}, q_{2,2}, p_{2,3}, q_{2,3}, p_{2,4}$	0, 1/9, 2/9, 1/3, 2/3, 7/9, 8/9, 1

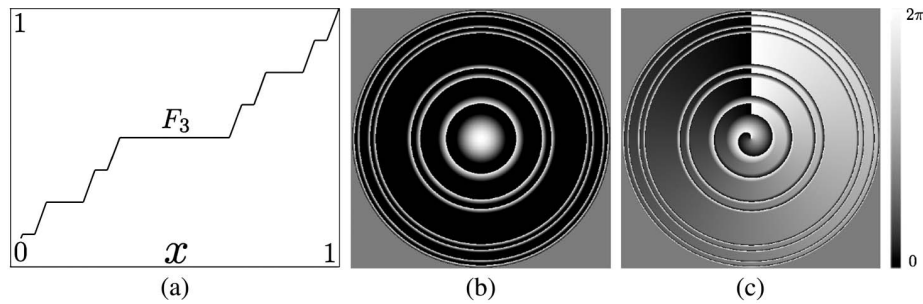


Fig. 1. (a) Plot of  $F_3(\zeta)$ . (b) Phase variation of  $\Phi_{3,0}(\sqrt{\zeta}, \theta)$ , which is a devil's lens or a DVL with a charge of 0. (c) Phase variation of  $\Phi_{3,1}(\sqrt{\zeta}, \theta)$ , which is a DVL with a vortex charge of 1.

DVFL. The diffraction pattern is calculated based on the Fresnel–Huygens wavelet approach using Coherent Optics [20]. Coherent Optics is a program for simulating laser illuminated optical systems and the construction of optical filters. Fig. 3(a) is the plot of the irradiance from a DVL with  $s = 3$  and  $m = 2$ . The  $z$  axis ranges from  $0 \rightarrow 6.85$  m, and the  $y$  axis from  $-665.5 \mu\text{m} \rightarrow 665.5 \mu\text{m}$ . At a distance of over 6 m, subsidiary foci are present. For ours and many other optical setups, this distance is too large. Fig. 3(b) is the plot of the same DVL with the addition of a Fresnel lens with a focal length of 1.3 m. The  $z$  has been shortened to range from  $0 \rightarrow 1.95$  m, while the  $y$  axis maintains the same scale  $[-665.5 \mu\text{m} \rightarrow 665.5 \mu\text{m}]$ . The focal structure is contained in a much smaller volume compared to Fig. 3(a). The majority of the diffracted energy is contained in the large focus located at  $z = 1.3$  m. Also, there are no foci at distances beyond  $z = 1.3$  m. The pattern is also more compact along the  $x$  and  $y$  axes.

### 3. DVFL Experiment

The laser system used for this experiment is a home-built Ti:sapphire femtosecond oscillator pumped by a Spectra-Physics Millennia at 3 W. The oscillator emits 50 fs pulses at an 80 MHz repetition rate with an average power of 150 mW. This beam has a center wavelength of roughly 800 nm. After exiting the oscillator cavity, the beam passes through a  $4f$  grating pair pulse shaper used for spectral dispersion compensation. After the pulse shaper, the laser (75 mW) is coupled into a microstructured fiber

(NKT Femtowhite 800) with a  $20\times$  microscope objective. This apparatus is used for other experiments in our lab utilizing the supercontinuum, but in the experiments presented here it is simply used as a spatial filter. The peak optical power is kept intentionally low (by operating the oscillator in the continuous-wave regime), thereby not generating any supercontinuum light. The output from the fiber then enters our SLM setup, shown in Fig. 4, where the rapidly diverging output from the fiber is collimated with an  $f = 70$  cm achromatic lens. This plane wave then impinges onto our reflective SLM, which is angled  $5.5^\circ$  off axis to send the return light back along a different path. Along this path, an optical rail system holds the CCD camera (Dataray Wincam-D), which is used to record the images.

This approach is advantageous since the small core of the fiber (approximately  $1 \mu\text{m}$ ) acts as an excellent point source. Combined with the relatively long focal length lens (70 cm), a very good plane wave is produced at the face of the SLM. This was confirmed by evaluating the collimated beam with a shear plate near the position of the SLM. Although this approach does not collect all the light from the fiber (the beam expands well beyond the 2 in. diameter of the lens), we have sufficient overhead optical power that this is not a major hindrance.

The SLM (Hamamatsu X8267-14) is a back-illuminated liquid-crystal-on-silicon design that eliminates pixilation and has a 100% fill factor. The reflective nature of this device is ideal for high-power beams (it can handle an amplified system as well). Our particular device is antireflection

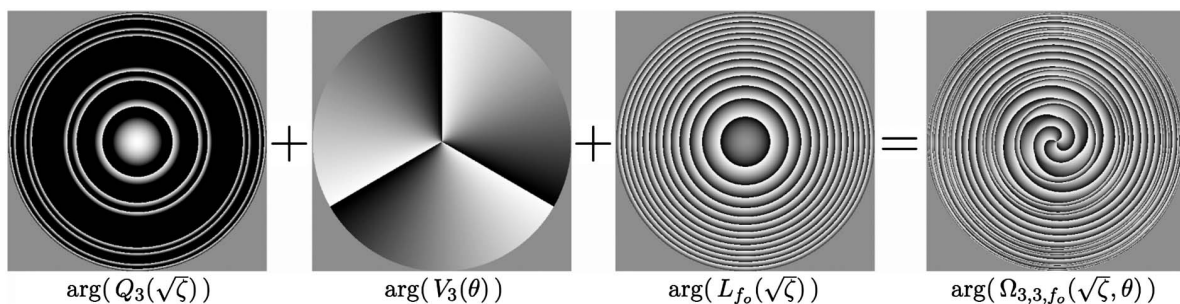


Fig. 2. Phase plots of each component that makes up a DVFL. The sum of all three phases, where  $s = 3$ ,  $m = 3$ , and  $f_0 = 4.62$  m, produces the final DVFL seen here.

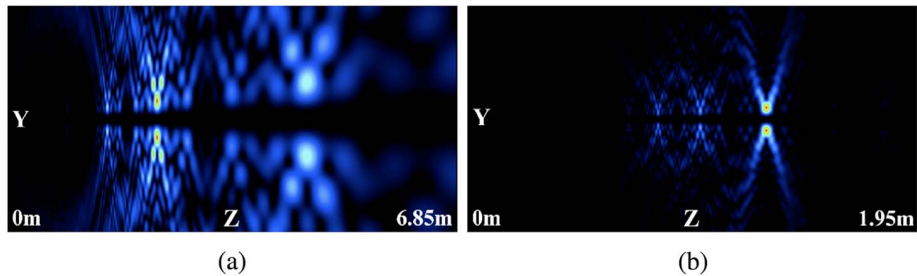


Fig. 3. (Color online) (a) Irradiance from a DVL with  $s = 3$  and  $m = 2$ , where the  $z$  axis goes from  $0 \rightarrow 6.85$  m. (b) Irradiance from the same DVL, but with the addition of a Fresnel lens with a focal length of  $1.3$  m. The  $y$  axis ranges from  $-665.5 \mu\text{m} \rightarrow 665.5 \mu\text{m}$  for both plots. The  $z$  axis goes from  $0 \rightarrow 1.95$  m. By incorporating a Fresnel lens, the diffracted light is contained in a much closer region.

coated for  $800$  nm, which means that it efficiently diffracts energy at this wavelength, and allows us to generate diffraction patterns in the zero order, as shown in Fig. 2. Other (less efficient) approaches generally require the use of a blazed grating on top of the desired pattern in order to move the overall diffraction pattern into the first-order diffracted beam.

The experimental procedure was then as follows. The SLM was calibrated to give  $2\pi$  modulation at our central wavelength, and the pattern shown in Fig. 2 was applied to the screen. The return light from the SLM propagated down an optical rail on which sat the CCD camera. This camera was moved manually to prescribed locations down the optical rail, and each image was recorded on the computer. Cross-sectional images and transverse projections versus  $z$  were generated as described in the Section 4.

#### 4. Experimental Results

The unique focal properties of the fractal zone plate lead to multiple longitudinal foci. In order to compare the measured intensity profiles with theory, we examined the cross-sectional images at the main focus and compared these to numerical predictions obtained with the Coherent Optics software package. In Fig. 5, we show the irradiance at the main focus,  $f_0 = 1.3$  m, for a DVFL of order  $s = 1$  to 4 and vortex charge  $m = 8$ . The top row shows the experimentally recorded images, and the bottom row shows the accompanying numerical predictions. As seen in the top row of Fig. 5, the experimental results, although slightly noisy, exhibit excellent agreement with the numerical results, both in the size and the

number of primary and secondary rings. We should note that, in these results, there was no scaling factor; the actual physical dimensions were entered into the numerical model.

In order to analyze the propagation of these beams, an entire series of CCD images was taken at increasing propagation distances from the SLM. The camera was first placed at  $623.7$  mm from the SLM, and an image was recorded, representing the cross-sectional irradiance profile of the beam. The camera was then moved  $1$  cm away to  $633.7$  mm, and another image was recorded. This process was repeated  $85$  times until we reached a distance of  $1463.7$  mm from the SLM. The photos were cropped such that everything was removed except a  $2$  pixel wide horizontal strip going through the center of the beam. The pictures were then placed side by side to create a transverse cross section of the beam. This new image was then expanded by a factor of  $3$  so that the slices become  $6$  pixels wide, which gives a total picture size of  $510$  pixels. We then cropped the width so that the final image has the dimensions  $512 \times 510$ . The calculations are done using a  $512 \times 512$  array and the Fresnel approximation. The range was purposely extended by an additional  $3.29$  mm so that the last  $2$  pixels of the calculations could be removed, leaving a plot that is  $512 \times 510$ , with a matching  $z$  range of  $[623.7 \text{ mm}, 1463.7 \text{ mm}]$ . The color mapping is such that the greatest intensity is mapped to red and the smallest mapped to black.

The experimental results in Fig. 6 (top row) show excellent agreement with the numerical predictions (bottom row). Each vortex is centered along a common optical axis, resulting in a dark core along the

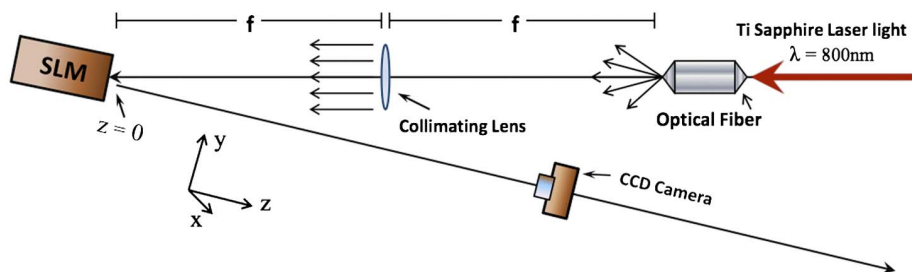


Fig. 4. (Color online) Schematic drawing of the optical setup used. The SLM is tilted to reflect the beam along the path away from the incident beam path.

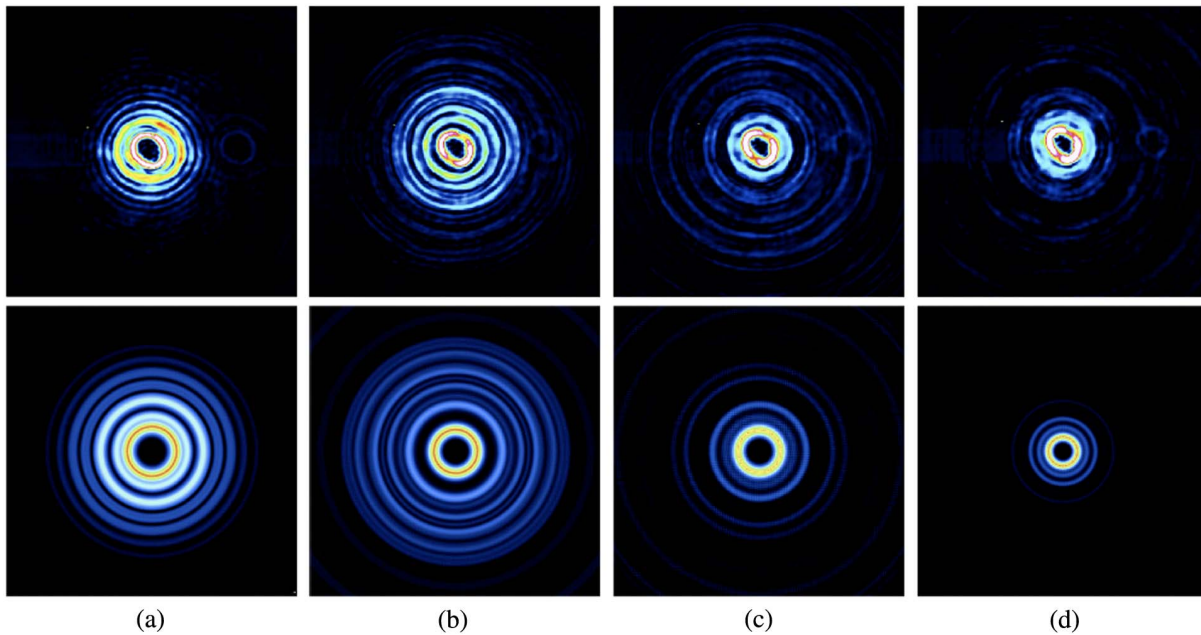


Fig. 5. (Color online) Side-by-side comparisons of the calculated cross-section irradiance (bottom row) versus experimental data (top row). (a)  $s = 1, m = 8$ ; (b)  $s = 2, m = 8$ ; (c)  $s = 3, m = 8$ ; (d)  $s = 4, m = 8$ . For each plot, both the  $x$  and  $y$  axes range from  $[-1331 \mu\text{m}, 1331 \mu\text{m}]$ .

laser propagation direction. As sequential vortices come into focus, we see that each vortex increases in size with distance from the SLM. For example, for  $s = 3$ , in Fig. 6(c), we see that each successive vortex has a slightly larger dark center. This is simply due to focusing with different focal length lenses. Using a short focal length lens will produce a smaller image (hence a smaller dark center) than using a longer focal length lens. The positions and transverse sizes of the primary and secondary foci match exceptionally

well, as expected. But what the careful reader will note is the amazing agreement in the wings of each image (the images were intentionally saturated at the primary focus to bring out the secondary fringes). In fact, the interference patterns match nearly perfectly down to the lowest intensity levels recorded. This is a testament to both (a) the optical setup, that the combination of small core fiber and long focal length lens makes an excellent plane wave, and (b) the quality of the SLM; the high resolution and

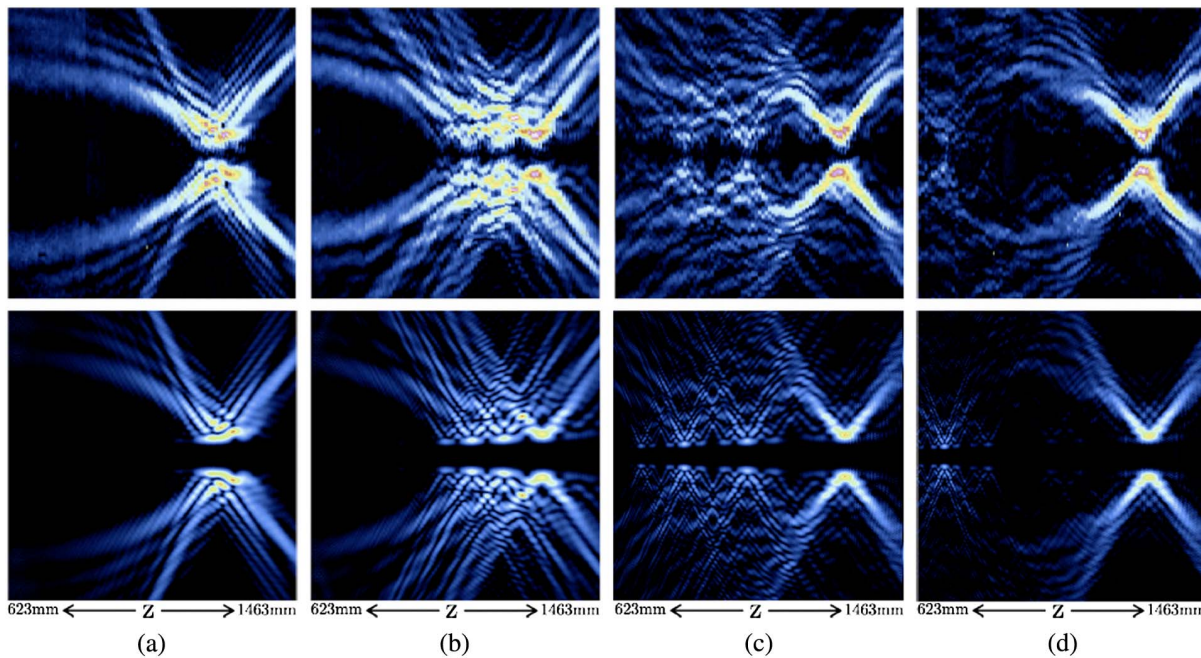


Fig. 6. (Color online) Side-by-side comparisons of calculated irradiance versus experimental data. Again, (a)  $s = 1, m = 8$ ; (b)  $s = 2, m = 8$ ; (c)  $s = 3, m = 8$ ; (d)  $s = 4, m = 8$ . For each plot,  $z$  ranges from  $[623 \text{ mm}, 1463 \text{ mm}]$ , and  $y$   $[-1331 \mu\text{m}, 1331 \mu\text{m}]$ .

lack of pixels contributes greatly to an improved image.

## 5. Conclusion

In this paper, we have presented the experimental realization of a DVL through the use of a programmable SLM. It is well known that the addition of a spiral phase will turn the foci of the field into vortices. By including a fractal zone plate with multiple foci, however, the vortex spot is able to occupy multiple positions along the optical axis. By also incorporating a Fresnel lens pattern on the SLM, the positions of the multiple vortices were modified to fit within a more compact region. The phase pattern was encoded modulo  $2\pi$ , making full use of the dynamic range of the SLM while maintaining the integrity of the complex phase patterns. Since no static refractive elements are used in our arrangement, the generated focal pattern is fully and dynamically adjustable. What is uniquely appealing in the results presented is the phenomenal agreement between the complex irradiance patterns observed in the laboratory and our numerical simulations. This not only demonstrates the high quality of the SLM and our optical setup but also the true power of the Huygens–Fresnel wavelet theory of propagation, captured numerically in the software used here. This predictive power of the theory lends significant weight to proposals for generating ever more complex irradiance patterns that could have potential applications in optical particle trapping and manipulation, microscopy, and quantum information research.

Note added in proof: Similar results have appeared recently [21].

## References

1. P. A. M. Dirac, "Quantised singularities in the electromagnetic field," *Proc. R. Soc. A* **133**, 60–72 (1931).
2. J. F. Nye and M. V. Berry, "Dislocations in wavetrains," *Proc. R. Soc. A* **336**, 165–190 (1974).
3. L. Allen, M. Beijersbergen, R. J. C. Spreeuw, and J. P. Woerdman, "Orbital angular momentum of light and the transformation of Laguerre–Gaussian laser modes," *Phys. Rev. A* **45**, 8185–8189 (1992).

4. N. R. Heckenberg, R. McDuff, C. P. Smith, and A. G. White, "Generation of optical phase singularities by computer-generated holograms," *Opt. Lett.* **17**, 221–223 (1992).
5. M. Reicherter, T. Haist, E. U. Wagemann, and H. J. Tiziani, "Optical particle trapping with computer-generated holograms written on a liquid-crystal display," *Opt. Lett.* **24**, 608–610 (1999).
6. K. T. Gahagan and G. A. Swartzlander, "Optical vortex trapping of particles," *Opt. Lett.* **21**, 827–829 (1996).
7. K. Ladavac and D. G. Grier, "Microoptomechanical pump assembled and driven by holographic optical vortex arrays," *Opt. Express* **12**, 1144–1149 (2004).
8. J. Leach, B. Jack, J. Romero, A. K. Jha, A. M. Yao, S. Franke-Arnold, D. G. Ireland, R. W. Boyd, S. M. Barnett, and M. J. Padgett, "Quantum correlations in optical angle–orbital angular momentum variables," *Science* **329**, 662–665 (2010).
9. S. Fürhapter, A. Jesacher, S. Bernet, and M. Ritsch-Marte, "Spiral phase contrast imaging in microscopy," *Opt. Express* **13**, 689–694 (2005).
10. I. Augustyniak, A. Popiolek-Masajada, J. Masajada, and S. Drobczyński, "New scanning technique for the optical vortex microscope," *Appl. Opt.* **51**, C117–C124 (2012).
11. M. R. Dennis, K. O'Holleran, and M. J. Padgett, "Singular optics: optical vortices and polarization singularities," in Vol. 53 of *Progress in Optics* (Elsevier, 2009), Chap. 5, pp. 293–363.
12. G. Saavedra, W. D. Furlan, and J. A. Monsoriu, "Fractal zone plates," *Opt. Lett.* **28**, 971–973 (2003).
13. J. A. Davis, L. Ramirez, J. A. Martn-Romo, T. Alieva, and M. L. Calvo, "Focusing properties of fractal zone plates: experimental implementation with a liquid-crystal display," *Opt. Lett.* **29**, 1321–1323 (2004).
14. S. H. Tao, x. C. Yuan, J. Lin, and R. Burge, "Sequence of focused optical vortices generated by a spiral fractal zone plate," *Appl. Phys. Lett.* **89**, 031105 (2006).
15. J. A. Monsoriu, W. D. Furlan, G. Saavedra, and F. Gimnez, "Devil's lenses," *Opt. Express* **15**, 13858–13864 (2007).
16. D. Wu, L. G. Niu, Q. D. Chen, R. Wang, and H. B. Sun, "High efficiency multilevel phase-type fractal zone plates," *Opt. Lett.* **33**, 2913–2915 (2008).
17. P. Bak, "The devil's staircase," *Phys. Today* **39**(12), 38–45 (1986).
18. D. R. Chalice, "A characterization of the Cantor function," *Am. Math. Mon.* **98**, 255–258 (1991).
19. W. D. Furlan, F. Gimnez, A. Calatayud, and J. A. Monsoriu, "Devil's vortex-lenses," *Opt. Express* **17**, 21891–21896 (2009).
20. D. Cottrell, "Coherent Optics freeware," <http://www-rohan.sdsu.edu/~dcottrel/>.
21. A. Calatayud, J. A. Rodrigo, L. Remón, W. D. Furlan, G. Cristóbal, and J. A. Monsoriu, "Experimental generation and characterization of Devil's vortex-lenses," *Appl. Phys. B* **106**, 915–919 (2012).